Innovative Infrastructure Solutions (2021) 6:37
https://doi.org/10.1007/s41062-020-00405-9

TECHNICAL PAPER

Different aspects of slope failures considering large deformation: application of smoothed particle hydrodynamics (SPH)

Md. Aftabur Rahman[1] · Nafisa Tabassum[1] · Mohammed Russedul Islam[2]

Received: 12 September 2020 / Accepted: 10 November 2020 / Published online: 26 November 2020

Abstract

Understanding the insight of slope collapse is necessary for effective hazard mitigation policy. The conventional method may not be able to capture the actual failure mechanics as these methods are based on simplified assumptions of the predetermined slip surface. Highlighting this real engineering problem, an attempt is made in this research to simulate different aspects of slope collapse numerically. Lagrangian particle-based continuum model, namely, smoothed particle hydrodynamics (SPH) has been used to develop a three-dimensional numerical slope model to understand the failure mechanics of unstable slopes. Both homogeneous and non-homogeneous slope models have been simulated, and the time history of naturally occurring failure planes has been tracked. A distinct slip surface has been seen from displacement contour of particles, which portray the innate response of a collapsed slope. The effect of soil properties on the response of slope surface has also been evaluated quantitatively by the different combination of non-homogeneous slope models. Afterwards, two conventional remedial measures have been simulated, and significant reduction of run-out length is seen, which can put a spotlight on future mitigation strategy in geotechnical hazard.

Keywords Slope · SPH · Homogeneous · Non-homogeneous · Countermeasure

Introduction

Landslide is one of the major geotechnical hazards and is extremely vulnerable in mountainous countries. Among several landslide types, shallow slide often refers as slope failure, is dangerous not only in the steep mountainous regions, but also equally destructive in small hillocks, roads, and embankments [1]. Typically, stability is measured in terms of factor of safety (FoS) to determine the susceptibility of possible collapse. Limit equilibrium method (LEM) has been used to evaluate the overall stability of slopes. To date, a significant number of LEM approaches has been formulated and used in practical applications of slope stability problems [2]. These LEM approaches usually assume a circular slip plane and factor of safety is calculated based on the assumed slip surface and geotechnical properties of soils within the slip surface. However, in reality, the collapse may not follow the same trend all the time of slope failures [3]. Instead, different factors such as triggering mechanics, soil properties, and geological formation play a vital role in determining the slip surface; hence, the typical LEM suffers a limitation in dealing with actual failure mechanics. Emphasizing on the shortcomings of LEM, researchers devoted to experimental investigations to know the insight of slope collapses [4–6]. The experimental findings put many information to understand the mechanics of slope failures, though, the discrepancy between model and prototype restricts the experiments in many cases.

On the other hand, computational facilities have been expanded significantly in the last decades and allow researchers and professionals to simulate real engineering problems [7]. In line with the trend, extensive numerical simulations in slope stability have been conducted in recent

✉ Md. Aftabur Rahman
maftabur@cuet.ac.bd

Nafisa Tabassum
nafisa_t@cuet.ac.bd

Mohammed Russedul Islam
russed@ce.mist.ac.bd

[1] Department of Civil Engineering, Chittagong University of Engineering & Technology, Chattogram 4349, Bangladesh

[2] Department of Civil Engineering, Military Institute of Science & Technology, Mirpur Cantonment, Dhaka, Bangladesh

years. Most of the researches are based on the Eulerian approach, while in reality, slope collapse belongs to large deformation and is hardly compatible with the Eulerian approach [7]. Besides that the Lagrangian approach can handle slope simulation as it can capture the large deformation process more accurately. There are several numerical methods developed in Lagrangian approach such as discrete element method (DEM), material point method (MPM), smoothed particle hydrodynamics (SPH), discontinuous deformation analysis (DDA) etc. Among several Lagrangian numerical methods, SPH is a particle-based continuum approach which has been formulated to capture the large deformation [8]. In SPH, there is no connectivity among the particles, and the ability to model complex geometry makes this numerical tool a robust one. Also, appropriate constitutive relations can be added to the governing equations of SPH, and therefore, the consideration of material behaviour is possible in this numerical model [9].

Furthermore, SPH has been successfully applied in large deformation geotechnical problems [10–13]. Considering all the affirmative nature of SPH, an attempt was taken in this research to develop a numerical model in SPH environment for slope failure analysis. A series of three-dimensional scaled numerical model was run to capture the realistic behaviour of slopes under both homogeneous and non-homogeneous properties. The post flow behaviour and possible estimation of maximum run-out, which are the ultimate goal for an effective prevention plan were extracted from numerical simulations. The naturally occurring slip plane was tracked, and the effect of different properties on the formation of slip surface was investigated. In addition, two conventional mitigation measures were numerically simulated to check their effectiveness in preventing possible disaster. The subsequent sections describe in detail the development and outcome of the numerical model.

Basic formulation of numerical model

Background of SPH

The first development of SPH was intended for solving astrophysical problems [14]. After the successful application of simulation of moving stars, this method extended to solve hydrodynamics problems, free surface simulations, wave overtopping and able to capture the behaviour of large deformation [11, 15–30]. Recently, researchers widen the application of SPH to solve geotechnical problems after the pioneering works of Bui and his co-researchers [31]. Debris flows and lahars were simulated in SPH, considering dilute characteristics of materials for many practical events, and successfully replicate the real instances [32–40]. Even this method has been used to know the insight of debris flow mechanics and velocity estimations for effective hazard mitigation [10, 41]. Overall, SPH is a robust and user-friendly numerical approach for solving complex geometries and large deformation analysis. The following section describes the formulation of SPH with necessary equations.

Fundamental of SPH

The basic formulation of SPH consists of the integral representation of field functions (kernel approximation) and the particle approximation. A set of finite discretized particles was used to represent the entire computational domain, which possesses volume and mass of the material, and also physical properties such as velocity, acceleration, density, stress, etc. The properties of every particle are updated in each computational step by averaging the properties of particles within a particular zone, called an influence zone. A smoothing kernel function was used to estimate the particle properties. Next, the particle approximation of the function was conducted by converting the continuous integral representations into discretized forms of summation over the nearest neighbouring particles. The basic formation of SPH is shown in the Fig. 1.

In the SPH method, the integral representation of a function can be expressed as follows:

$$f(x) = \int_{\Omega} f(x')\delta(x - x')\mathrm{d}x' \tag{1}$$

where $f(x)$. represents a function of the three-dimensional position vector x, Ω is the volume of the integral which holds

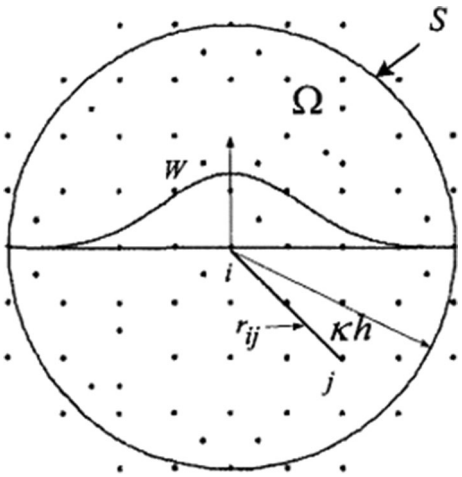

Fig. 1 Particle approximations using particles within the support domain of the smoothing function W for *particle i*

x. and $\delta(x-x')$ is the Dirac Delta function. This Dirac Delta function is given by,

$$\delta(x-x') = \begin{cases} 1 & x = x' \\ 0 & x \neq x' \end{cases}. \tag{2}$$

The continuous SPH integral representation for $f(x)$. can be expressed as the following discretized particle approximation form.

$$f(x) = \sum_{j=1}^{N} \frac{m_j}{\rho_j} f(x_j) W(x - x_j, h) \tag{3}$$

Similarly, the particle approximation for the spatial derivative of the function is

$$\nabla \cdot f(x) = \sum_{j=1}^{N} \frac{m_j}{\rho_j} f(x_j) \cdot \nabla W(x - x_j, h) \tag{4}$$

Where, the smoothing function W and its gradient ∇W are taken with respect the particle j.

Finally, for a given particle i, the particle approximation for a function and its spatial derivative at particle i can be expressed as:

$$\langle f(x_i) \rangle = \sum_{j=1}^{N} \frac{m_j}{\rho_j} f(x_j) \cdot W_{ij} \tag{5}$$

$$\text{Where, } W_{ij} = W(x_i - x_j, h) = W\left(\left|x_i - x_j\right|, h\right) \tag{6}$$

$$\langle \nabla \cdot f(x_i) \rangle = \sum_{j=1}^{N} \frac{m_j}{\rho_j} f(x_j) \cdot \nabla_i W_{ij} \tag{7}$$

$$\text{Where, } \nabla_i W_{ij} = \frac{x_i - x_j}{r_{ij}} \frac{\partial W_{ij}}{\partial r_{ij}} = \frac{x_{ij}}{r_{ij}} \frac{\partial W_{ij}}{\partial r_{ij}} \tag{8}$$

Where r_{ij} indicates the distance between particle i and j.

Different types of smoothing functions are available for implementation in the SPH literature. Each kernel function has its special feature to use in particular problems. A set of trial simulations was carried out and it was found that the most widely used cubic spline function, proposed by Monaghan and Lattanzio [42] provide better approximation of slope stability problems. The mathematical formulation of the kernel function is given in the following equation:

$$W_{ij} = \alpha_d \begin{cases} \frac{2}{3} - q^2 + \frac{1}{2}q^3 & 0 \le q < 1 \\ \frac{1}{6}(2-q)^3 & 1 \le q < 2 \\ 0 & q \ge 2 \end{cases} \tag{9}$$

where $\alpha_d = \frac{3}{2\pi h^3}$, $q = \frac{r_{ij}}{h} = \frac{x_i - x_j}{h}$ = the normalized/relative distance between particles i and j. The kernel function drops to zero for $\left|r_{ij}\right| \ge 2h$, implying that the influence domain in Eq. (9) has a radius of $2h$.

Derivative of cubic spline kernel function is written as,

$$\nabla_i W_{ij} = \alpha_d \begin{cases} \frac{X_{ij}}{r_{ij} h_{ij}} \left(-2q + \frac{3}{2}q^2\right) & 0 \le q < 1 \\ \frac{-X_{ij}}{2h_{ij} r_{ij}} (2-q)^2 & 1 \le q < 2 \\ 0 & q \ge 2 \end{cases} \tag{10}$$

Navier–Stokes equations are the governing equations in the SPH model, and these equations were solved by Leap-Frog numerical integration scheme to update the current particle position. This procedure continued until the sufficient convergence or target achieved for a particular purpose. The SPH version of governing equations in terms of continuity and momentum equations for a particle is:

$$\frac{D\rho_i}{Dt} = \sum_{j=1}^{N} m_j \left(v_i^{\alpha} - v_j^{\alpha}\right) \frac{\partial W_{ij}}{\partial x_i^{\alpha}} \tag{11}$$

$$\frac{Dv_i^{\alpha}}{Dt} = \sum_{j=1}^{N} m_j \left(\frac{\sigma_i^{\alpha\beta}}{\rho_i^2} + \frac{\sigma_j^{\alpha\beta}}{\rho_j^2} \right) \frac{\partial W_{ij}}{\partial x_i^{\beta}} + g_i^{\alpha} \tag{12}$$

where $\sigma^{\alpha\beta}$. is the total stress tensor, which can be described by appropriate constitutive relations, v_i is the velocity, g_i is the gravitational acceleration.

Constitutive modelling

The ideal representation of material behaviour is the most challenging task in the numerical application. Soil, which is a mixture of a wide range of solid particles, water and air are close to impossible to formulate in numerical scheme realistically. For large debris flow and earth flows, the slurry behaviour of debris mass often characterized by different viscous model. However, in shallow slope stability analysis, the application of viscous model may not be suited as the detached behaviour do not portray actual dilute characteristics. Besides, the mixture model considers the behaviour of solid and water phase, and the interaction between the components of soils are considered. However, numerical computation is complicated, and the stability of the simulation is a significant concern in such a case. In addition, the rationality for real slope simulation is not appropriately guaranteed. On the other hand, a simplified solid model somewhat replicates the behaviour of geo-materials rationally. From that viewpoint, solid elastic modelling can be incorporated, and formulation is straightforward in numerical computation. However, the element test on soil samples pointed out the

elastoplastic behaviour of geo-materials. Therefore, elastoplastic Drucker-Prager model, which has been used extensively in the geotechnical applications, was considered in the current study to characterize the soil behaviour.

For an elastic–perfectly plastic material, strain rate tensor ($\dot{\varepsilon}^{\alpha\beta}$.) is decomposed into an elastic strain rate tensor $\dot{\varepsilon}_e^{\alpha\beta}$ and plastic strain rate tensor $\dot{\varepsilon}_p^{\alpha\beta}$:

$$\dot{\varepsilon}^{\alpha\beta} = \dot{\varepsilon}_e^{\alpha\beta} + \dot{\varepsilon}_p^{\alpha\beta} \tag{13}$$

The elastic strain rate tensor $\dot{\varepsilon}_e^{\alpha\beta}$ is calculated by the generalized Hooke's law:

$$\dot{\varepsilon}_e^{\alpha\beta} = \frac{\dot{s}^{\alpha\beta}}{2G} + \frac{1-2\vartheta}{3E}\dot{\sigma}^{\gamma\gamma}\delta^{\alpha\beta} \tag{14}$$

where $\dot{s}^{\alpha\beta}$ is the deviatoric shear stress rate tensor; $\vartheta.$ = Poisson's ratio; $E.$ = Young's modulus; $G.$ = the shear modulus and $\dot{\sigma}^{\gamma\gamma}$ = sum of the three normal stress rate components, i.e. $\dot{\sigma}^{\gamma\gamma} = \dot{\sigma}^{xx} + \dot{\sigma}^{yy} + \dot{\sigma}^{zz}$

By using the plastic flow rule, the plastic strain rate tensor $\dot{\varepsilon}_p^{\alpha\beta}$. is given by,

$$\dot{\varepsilon}_p^{\alpha\beta} = \dot{\lambda}\frac{\partial g}{\partial \sigma^{\alpha\beta}}. \tag{15}$$

where $\dot{\lambda}.$ is the rate of change of plastic multiplier and $g.$ is the plastic potential function.

After some trivial calculations, the following is the final stress–strain relation considering positive stress rate

$$\dot{\sigma}^{\alpha\beta} = \sigma^{\alpha\gamma}\dot{\omega}^{\beta\gamma} + \sigma^{\gamma\beta}\dot{\omega}^{\alpha\gamma} + 2G\dot{e}^{\alpha\beta} + K\dot{\varepsilon}^{\gamma\gamma}\delta^{\alpha\beta} - \dot{\lambda}\left[3\alpha_\psi K\delta^{\alpha\beta} + \frac{G}{\sqrt{J_2}}s^{\alpha\beta}\right]. \tag{16}$$

$$\text{where, } \dot{\lambda} = \frac{3\alpha_\phi K\dot{\varepsilon}^{\gamma\gamma} + \left(G/\sqrt{J_2}\right)s^{\alpha\beta}\dot{\varepsilon}^{\alpha\beta}}{9\alpha_\phi\alpha_\psi K + G} \tag{17}$$

where $\sigma^{\alpha\beta} = s^{\alpha\beta} + \frac{1}{3}\sigma^{\gamma\gamma}\delta^{\alpha\beta}$ is the total stress tensor, $\dot{e}^{\alpha\beta} = \dot{\varepsilon}^{\alpha\beta} - \frac{1}{3}\dot{\varepsilon}^{\gamma\gamma}\delta^{\alpha\beta}$ is the deviatoric shear strain rate tensor, $\dot{\sigma}^{\gamma\gamma} = \dot{\sigma}^{xx} + \dot{\sigma}^{yy} + \dot{\sigma}^{zz}$ is the sum of the three normal stress rate on, $\dot{\varepsilon}^{\gamma\gamma} = \dot{\varepsilon}^{xx} + \dot{\varepsilon}^{yy} + \dot{\varepsilon}^{zz}$ is the sum of the three normal strain rate components, $K = \frac{E}{3(1-2\vartheta)}$ is the elastic bulk modulus, G = $\frac{E}{2(1+\vartheta)}$ is the shear modulus

Drucker-Prager yield criteria

The yield condition $\left(I_1, J_2\right)$ of Drucker-Prager model is expressed as follows:

$$f\left(I_1, J_2\right) = \sqrt{J_2} + \alpha_\phi I_1 - k_c = 0 \tag{18}$$

where I_1 is the first invariant of stress tensor, and J_2 is the second invariant of the deviatoric stress tensor and calculated by:

$$I_1 = \sigma^{xx} + \sigma^{yy} + \sigma^{zz} \tag{19}$$

$$J_2 = \frac{1}{2}s^{\alpha\beta}s^{\alpha\beta} \tag{20}$$

For 3D condition, the Drucker-Prager constants are computed by,

$$\alpha_\phi = \frac{2\sin\phi}{\sqrt{3}(3-\sin\phi)}; \quad k_c = \frac{6c\cos\phi}{\sqrt{3}(3-\sin\phi)} \tag{21}$$

Finally, the SPH formulation of constitutive equation considering non-associated flow rule at a given particle i is:

$$\frac{D\sigma_i^{\alpha\beta}}{Dt} = \sigma_i^{\alpha\gamma}\dot{\omega}_i^{\beta\gamma} + \sigma_i^{\gamma\beta}\dot{\omega}_i^{\alpha\gamma} + 2G\dot{e}_i^{\alpha\beta} + K\dot{\varepsilon}_i^{\gamma\gamma}\delta_i^{\alpha\beta} - \dot{\lambda}_i\left[3\alpha_\psi K\delta^{\alpha\beta} + \frac{G}{\sqrt{J_2}}s_i^{\alpha\beta}\right]. \tag{22}$$

$$\text{where, } \dot{\lambda}_i = \begin{cases} \frac{3\alpha_\phi K\dot{\varepsilon}_i^{\gamma\gamma} + \left(G/\sqrt{J_2}\right)s_i^{\alpha\beta}\dot{\varepsilon}_i^{\alpha\beta}}{9\alpha_\phi\alpha_\psi K + G} & f\left(I_1, J_2\right) > 0 \\ 0 & f\left(I_1, J_2\right) \le 0 \end{cases} \tag{23}$$

The final SPH formulations of the strain and spin rate tensors of a particle i are:

$$\dot{\varepsilon}_i^{\alpha\beta} = \frac{1}{2}\left(\frac{\partial v^\alpha}{\partial x^\beta} + \frac{\partial v^\beta}{\partial x^\alpha}\right) = \frac{1}{2}\left[\sum_{j=1}^{N}\frac{m_j}{\rho_j}\left(v_j^\alpha - v_i^\alpha\right)\frac{\partial W_{ij}}{\partial x_i^\beta} + \sum_{j=1}^{N}\frac{m_j}{\rho_j}\left(v_j^\beta - v_i^\beta\right)\frac{\partial W_{ij}}{\partial x_i^\alpha}\right]. \tag{24}$$

$$\dot{\omega}_i^{\alpha\beta} = \frac{1}{2}\left(\frac{\partial v^\alpha}{\partial x^\beta} - \frac{\partial v^\beta}{\partial x^\alpha}\right) = \frac{1}{2}\left[\sum_{j=1}^{N}\frac{m_j}{\rho_j}\left(v_j^\alpha - v_i^\alpha\right)\frac{\partial W_{ij}}{\partial x_i^\beta} - \sum_{j=1}^{N}\frac{m_j}{\rho_j}\left(v_j^\beta - v_i^\beta\right)\frac{\partial W_{ij}}{\partial x_i^\alpha}\right] \tag{25}$$

Validation

Prior to applying slope simulations, a benchmark test was conducted to validate the proposed numerical model. There are various experimentally obtained run-out data available in other SPH works till to date which could be used here to validate our current research work. The experiments of

granular column collapse conducted by Lube et al. [43] for different aspect ratios were simulated numerically in this research. Aspect ratio is defined as the ratio of initial height to initial length. Smaller aspect ratios are generally found in landslides induced slope collapse and related problems. However, to check the versatility of the developed model, a wide range of granular column collapse was simulated. The simulation was conducted in a dam break manner where flow started instantaneously once the gates were lifted. Particle flowed over the larger base and simulation was continued till the termination of velocities of maximum particles. The time history of the flow profiles was recorded, and the final run-out and height were used to compare the results. Figure 2 shows the maximum run-out of the collapsed column at different aspect ratios. Almost identical responses compare to the experiments were evident in the developed numerical model. The final flow height was also found compatible with the experiments. Hence, the proposed model can effectively replicate a benchmark test and justified for further application of the developed model.

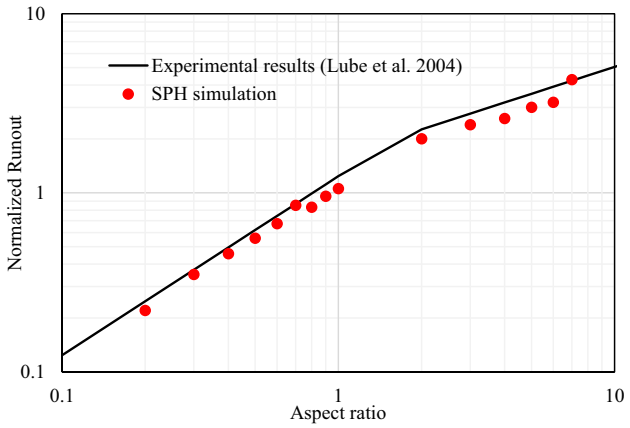

Fig. 2 Comparison of normalized final run-out between SPH simulations and experiments

Numerical modelling of slopes

A three-dimensional slope model was constructed using approximately 40,000 discrete particles with a spacing of 0.010 m between each particle. Aspect ratio is an important parameter in landslide induced slope failures, and a smaller aspect ratio was found in most of the long travelling flow [44]. Slope failure is also a type of landslides, and the aspect ratio is important in the modelling of the numerical slope. A much smaller aspect ratio is desirable for better accuracy of the simulation, though the increased computational cost may hinder in using minimal aspect ratio. An aspect ratio of 0.42 was chosen in the current study considering the real scenario and literature studies. Initially, particles were arranged in a square pattern for the formation of base. Then, particles placed to model a slope with 1.5H: 1 V gradient. The layout of the proposed slope model is shown in Fig. 3. Gravity was applied to all particles to consider overburden stress, and subsequently, particles started flowing following the governing equations with the elastoplastic constitutive model. The simulation was continued till the termination of flow, i.e. velocity dropped to zero for almost all particles. The time history of slope front was tracked as well as free-surface was recorded at a specific interval. Furthermore, time history of velocities of particles were recorded and checked before deciding the termination of the simulation. For some

Fig. 3 Geometry of slope model

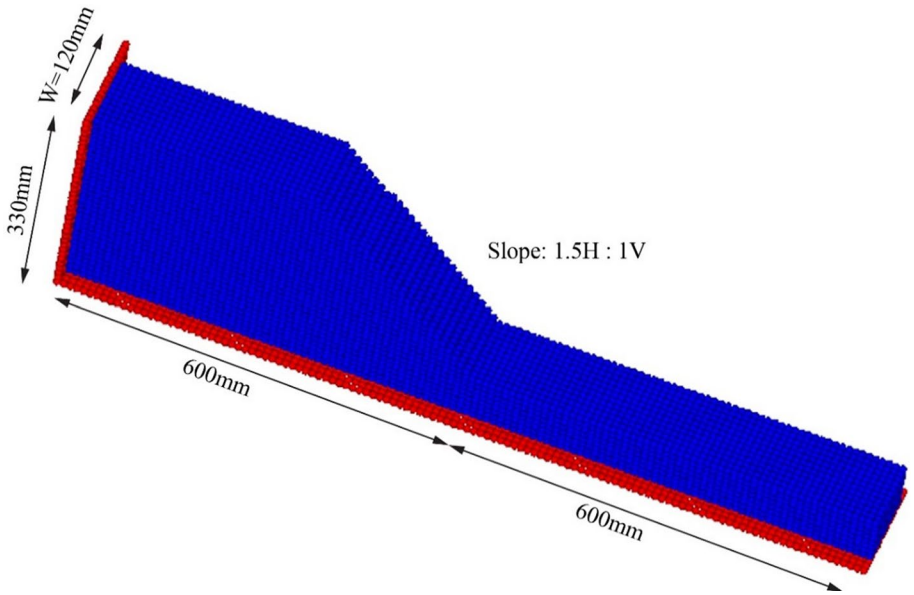

trial simulations, it was found that velocities dropped significantly after 6.0 s of flow. However, to observe the actual run-out and slope profile, the simulation was continued to 8.0 s for all cases.

Periodic boundary condition was applied across the smaller side of the slope to account for more realistic three-dimensional behaviour of slope model. That means a particle beyond one side of the slope in short direction entered into the opposite side. Therefore, the constraint owing to the boundary condition was skipped. The bottom and sidewall of the slope were kept fixed. However, the front length after the termination of the slope is an important dimension on the response of slope. In reality, this length is an infinite media and considering infinite extent is beyond the scope of the numerical or experimental procedure. A sufficient larger front length provides a more accurate response, and therefore, the sensitivity of this length was conducted prior to selecting it as equal to the base length of the slope. The subsequent section describes the effect of front length on the response slope collapse.

Effect of front length

As discussed in the previous section, the front length of the model after the termination of the slope is important from the numerical point of view. Therefore, a sensitivity study was taken prior to the simulation of the developed model. A three front length equal to 50% of the base length (300 mm), 100% of the base length (600 mm), and 150% of the base length (900 mm) was simulated for a typical granular slope. The layout of the model for sensitivity analysis is shown in Fig. 4. Flow profile, as well as the front part of the collapsed slope, was tracked for all cases. Final slope profile of all cases is shown in Fig. 5. It was found that the maximum run-out of all cases were somewhat similar, hence reveal the less significant effect on the run-out length estimation. The trend of the final profile was also alike among the three cases. To further observe their effect, displacement contour of particles was plotted in Fig. 6. The effect of front length was visible in Fig. 6, where base particles suffered significant displacement for shorter base length (Fig. 6a), while much fewer base particles were displaced for larger front length (Fig. 6b, c). Comparing all three responses, the front length equal to the base of the slope was compatible, and the effect of boundary condition reduced in a great deal. Therefore, the front length of 600 mm, chosen in the current study, was justified.

Results and discussions

Discussion on response of homogeneous slopes

The slope model shown in Fig. 3 was used for homogeneous slope simulation. Both granular and cohesive soils were simulated through the developed model. Cohesion was zero in case of granular soils, while a specific cohesion was used for cohesive soils. Frictional angle was constant in both simulations; therefore, the effect of cohesion can be distinctive from the simulations. The properties of homogeneous soil slopes are shown in Table 1.

Run-out length is a practical parameter for landslides and slope failure disaster evaluation as well as for mitigation strategy. The response of slopes was plotted in terms

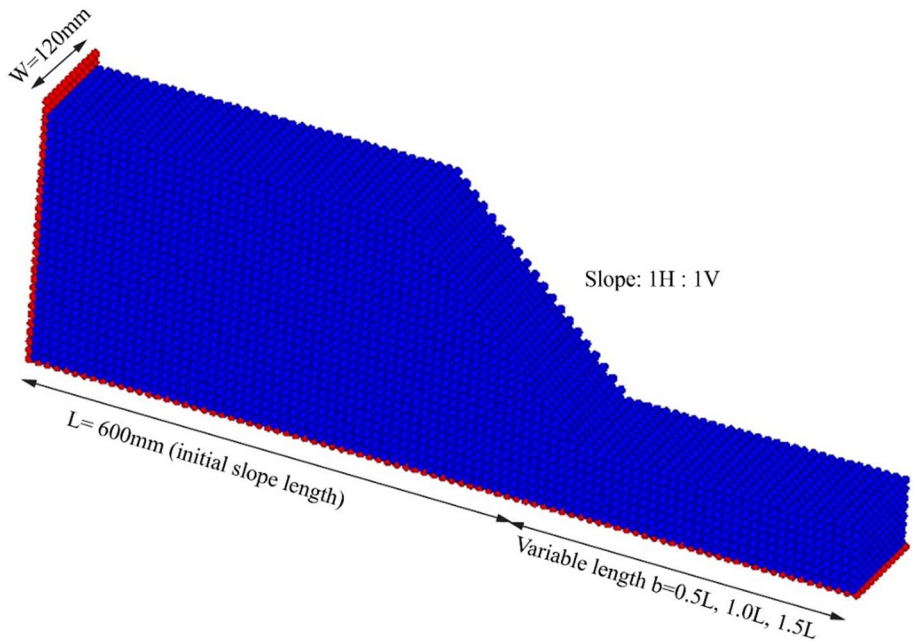

Fig. 4 Geometry of slope for effect of boundary condition

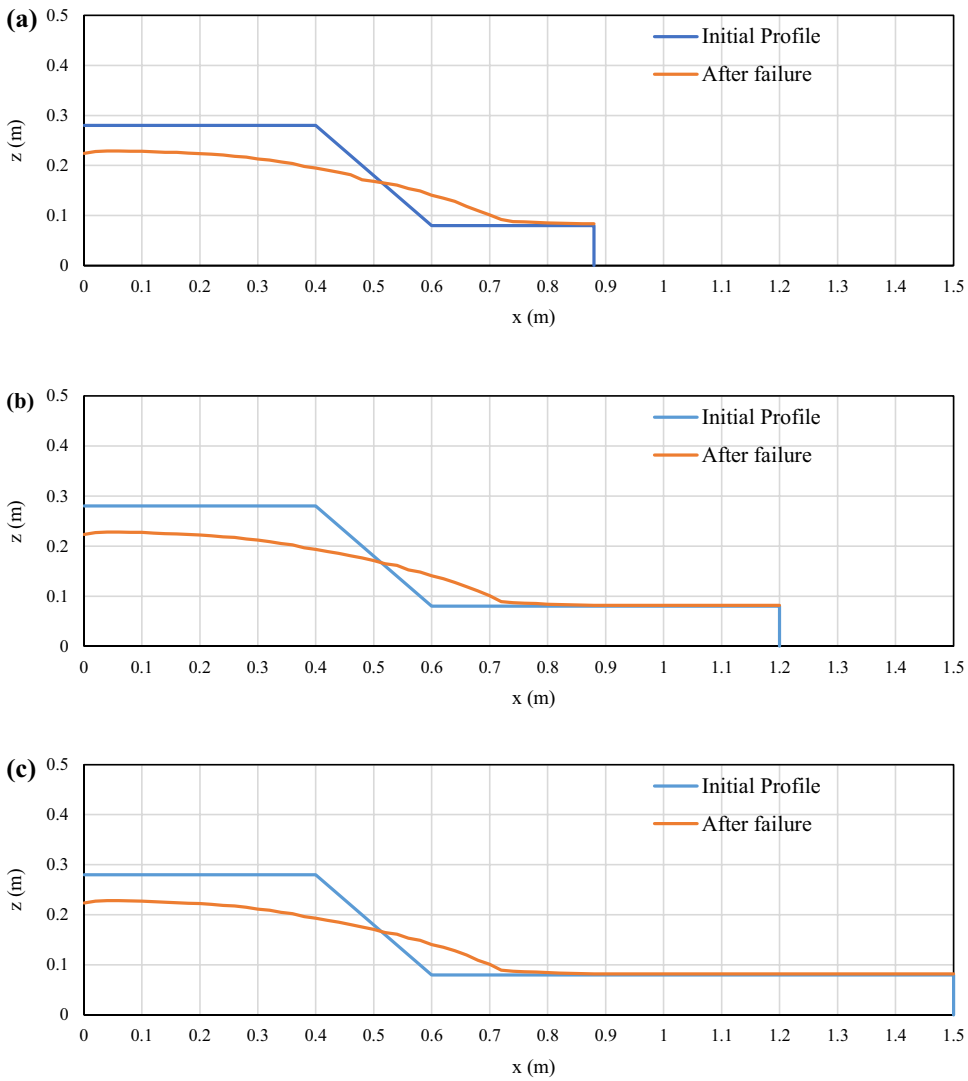

Fig. 5 Slope profile for different front length: **a** when b = 0.3 m (50% of initial base length), **b** when b = 0.6 m (100% of initial base length), **c** when b = 0.9 m (150% of initial base length)

of its normalized run-out length in the current study. The run-out length was normalized to the initial base length following the assumption that the maximum energy released instantaneously after the collapse and subsequently, residual flow occurs as discussed by Rahman [44]. The time history of normalized run-out for both granular and cohesive soil slopes was plotted in Fig. 7. The run-out distance was found to increase rapidly from 0 s to 1 s. The normalized run-out value was about 0.4 for granular soils and about 0.13 for cohesive soils at 1 s of simulation. After 1 s, run-out followed a straight-line trend for both types of soil and reached a somewhat stable condition at 8 s without any sudden increase in value. Run-out of cohesive soil slopes was much less compared to granular soil, assuming that cohesion act as a resistance to the collapse of the soil mass. The consistency of the initial peak of the run-out was further evident from the velocity response of particles for both granular and cohesive soil slopes, shown in Figs. 8 and 9 respectively. From the figures, a toe failure type is observed in both cases. Failure is initiated from the toe, and it emerges upwards, forming a circular failure pattern. For both granular & cohesive soils, velocity profiles depict an initiation of a failure surface from the toe at 0.1 s. There is an increase in velocity observed from 0.1 s to 0.2 s. At 0.2 s, this failure surface emerges to the top surface from the toe delineating a circular failure plane for both granular soils and cohesive soils. The red band distinguishably marks the failure planes. At 0.5 s, it was found that there was a considerable decrease in velocity. The maximum velocity portion (red band) was seen to decrease in velocity profile showing a thinner plane failure surface than before in case of granular soil. In the case of cohesive soil, velocity was quite reduced (green band rather than the red band) with a thinner plane failure surface at 0.5 s, indicating a stable condition was approaching. The velocity significantly reduced after 1 s, showing the profile with maximum particle marked by blue band distribution.

The final slope profile plotted in Fig. 10 demonstrated a much steeper repose angle for cohesive soils, while smaller

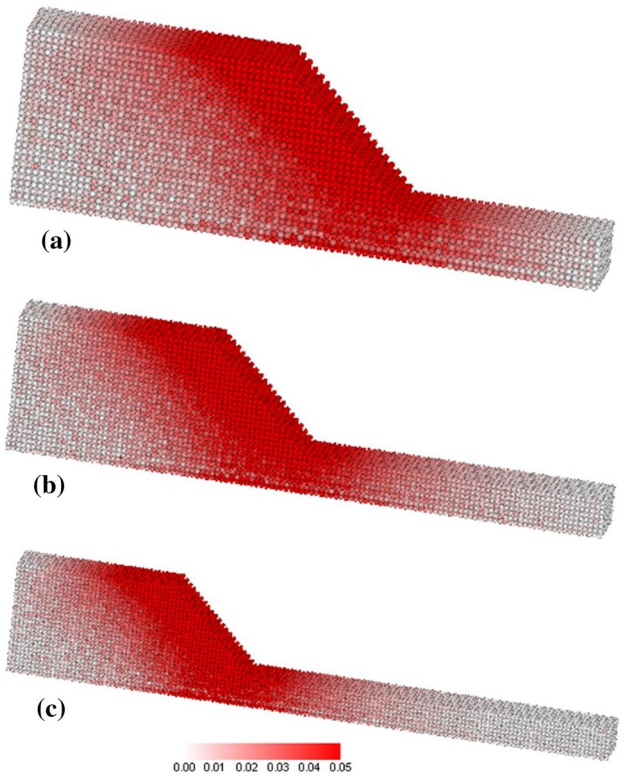

Fig. 6 Displacement contour of slopes for different front length: **a** when b = 0.3 m (50% of initial base length), **b** when b = 0.6 m (100% of initial base length), **c** when b = 0.9 m (150% of initial base length)

Table 1 Properties of homogeneous slopes

Parameter	Unit	Granular soils	Cohesive soils
Particle size (dx)	mm	10	10
Number of particles	–	28,171	28,171
Density (ρ)	kg/m^3	1800.0	1800.0
Cohesion (c)	kPa	0.0	10.0
Friction angle (φ)	Degree	17.5	17.5
Modulus of elasticity (E)	kPa	100	100
Poisson ratio (ν)	–	0.25	0.25

repose angle was seen for granular slope collapse. Furthermore, the height of slopes with granular soils is found to decrease than slope with cohesive soils since the more significant movement of soil mass took place in the run-out direction for granular soils.

Generally, a slip plane was approximated in conventional slope stability analysis which may not replicate the real instances. Highlighting this issue, this research aimed to plot the displacement contour of final slope particles and shown in Fig. 11. The highly displaced particle showed a dark red band which is almost similar to assumed slip plane in the conventional analysis. The displaced soil particles

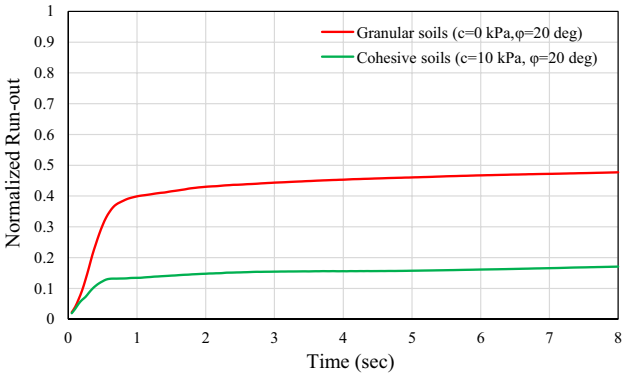

Fig. 7 Normalized run-out of failed slope with homogeneous properties

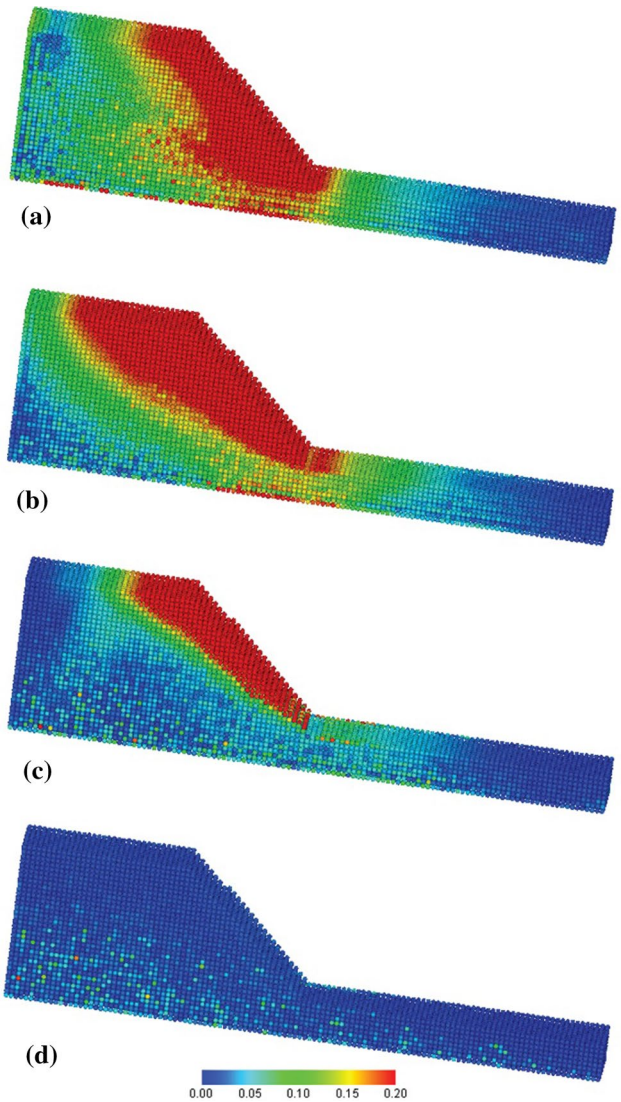

Fig. 8 Velocity distribution at different times for granular soils: **a** at t = 0.1 s, **b** at t = 0.2 s, **c** at t = 0.5 s, **d** at t = 1.0 s

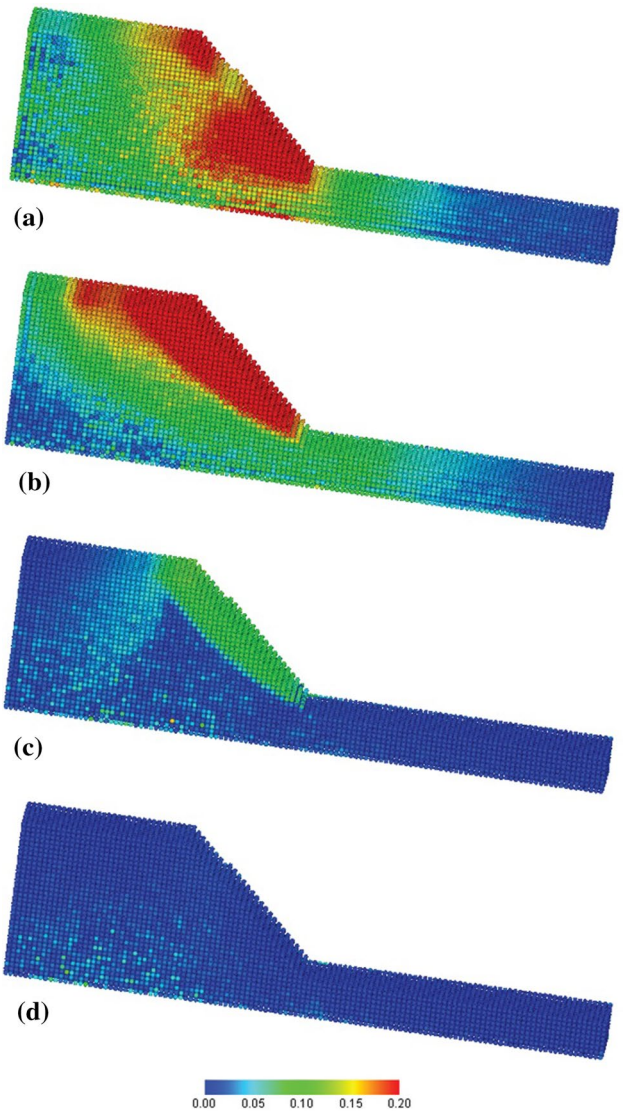

Fig. 9 Velocity distribution at different times for cohesive soils: **a** at t = 0.1 s, **b** at t = 0.2 s, **c** at t = 0.5 s, **d** at t = 1.0 s

naturally formed such a slip plane and can be considered to detect susceptible region in slope stability analysis so that proper ground anchoring or any other mitigation policy can be effectively taken. An extended failure plane was seen for granular soils, hence depict the reason of larger run-out for such soil.

Discussion on response of non-homogeneous slopes

For natural slopes, the soil properties are not homogeneous; rather, their properties vary with the depth. The response of such non-homogeneous slopes is an important index in the slope failure simulation. A series of SPH simulations of non-homogeneous soil slopes were conducted in the present research. The model was divided into three regions: a base layer comprises all base particles including boundary particles, a middle layer, and a top layer. A total of five combinations were considered for this study. Base soil properties kept same for all combinations, while the engineering properties of soils of both middle and top layer changed in each case. The case-1 is a typical non-homogeneous slope model, where the top layer is cohesive soil over a loose sandy layer. The case-2 and case-3 were granular assemblies with alternate soil properties, i.e. comparatively dense sandy soils were placed over loose sandy soils in case-2, while the opposite combination was used in case-3. In case-4, both layers consist of cohesive soil though the upper layer was a bit susceptible with low cohesion parameters, and the vice versa was seen in case-5. The other properties remained the same, and fundamental properties are listed in Table 2. A general layout for non-homogeneous slope model is shown in Fig. 12.

The normalized run-out and displacement contour of different non-homogeneous slope models were depicted in Figs. 13 and 14, respectively. The distinctive nature of each combination was seen from their time history response. For non-homogeneous granular slope models (slope-2), the loose middle sandy soils were responsible for significant damage as run-out was huge compare to the different properties. Usually, the collapse initiated from the toe of the slope, which eventually contributes to the damage and possible long run-out. Likewise, a loose middle sandy layer was responsible for the large run-out of the slope-2, and at the same time, the presence of comparatively dense soils at

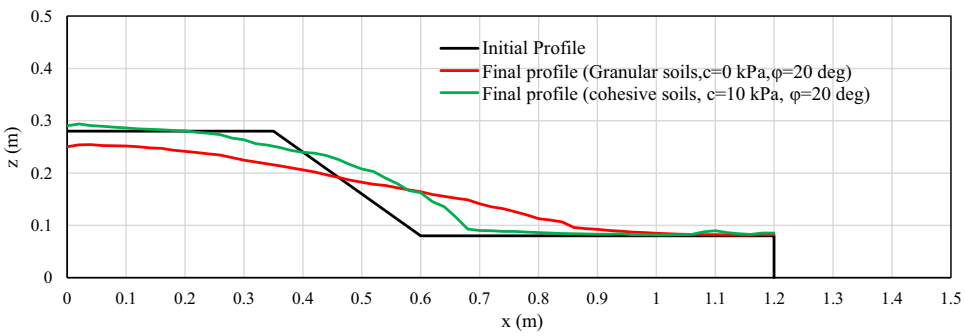

Fig. 10 Final slope profile for different types of soils with homogeneous properties

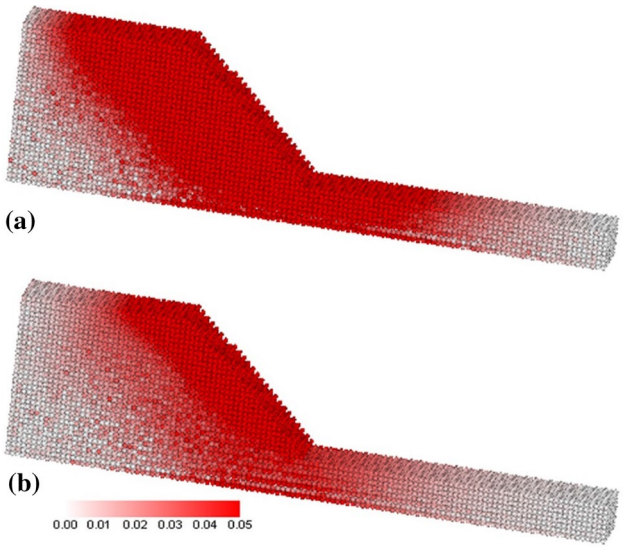

Fig. 11 Displacement contour of different soil types: **a** Granular soils, **b** Cohesive soils

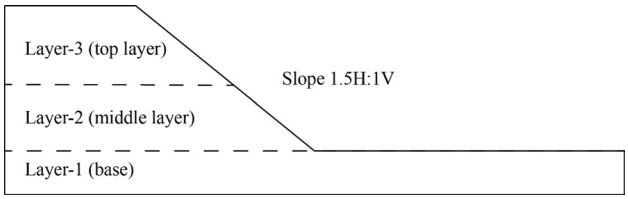

Fig. 12 Initial slope geometry for non-homogeneous slope simulation

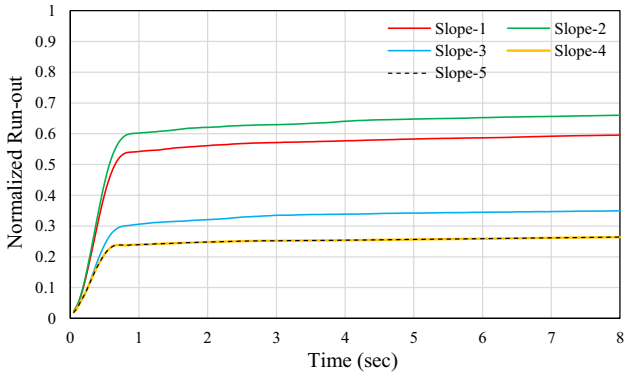

Fig. 13 Normalized run-out for different non-homogeneous slopes

toe reduces the run-out length in a great deal, approximately almost 50%. Besides, a smooth slip plane in terms of displaced mass was observed for slope model-2 in Fig. 14b, while the narrowband was seen for slope model − 3 in Fig. 14c. It was found that the variation of properties leads to change both the shape and extent of failure plane, which cannot be captured in conventional LEM, while the currently developed model can naturally locate the susceptible zone for slope failures. Besides that the different cohesive properties were not found significant in terms of run-out length. Almost identical run-out was observed for both slope-4 and slope-5. However, the comparison was difficult as both friction and cohesion parameters influence the slope collapse in cohesive slope failures. The reason for using frictional parameters was that in reality, some friction exists even in cohesive soil particles. Probably, the cohesive parameters dominate the flow patterns, and therefore, no significant discrepancy in terms of run-out was observed. Though the variation was not distinctive from the run-out perspective, a difference in the slip plane was seen in Fig. 14d and e. Extended slip plane was seen in slope-4, while the band was narrow in slope-5. In general, the proposed model capable of handling slope deformation and the affirmative essence is the development of inherent slip plane, which could be a key for proper anchoring for mitigation of shallow slope collapse.

Remedial measures in slope protection

The preceding sections describe the inherent features of both homogeneous and non-homogeneous slope failures. This disaster can be prevented, or the destruction can be

Table 2 Properties of non-homogeneous slopes

Layer	Parameter	Unit	Slope-1	Slope-2	Slope-3	Slope-4	Slope-5
Layer-3 (top layer)	Cohesion (c)	kPa	8.5	0.0	0.0	8.5	18.0
	Friction angle (φ)	Degree	14.0	20.0	14.0	14.0	18.0
	Poisson ratio (ν)	–	0.22	0.22	0.22	0.22	0.22
Layer-2 (middle layer)	Cohesion (c)	kPa	0.0	0.0	0.0	18.0	8.5
	Friction angle (φ)	Degree	15.0	14.0	20.0	18.0	14.0
	Poisson ratio (ν)	–	0.22	0.22	0.22	0.22	0.22
Layer-1 (base)	Cohesion (c)	kPa	20.0	20.0	20.0	20.0	20.0
	Friction angle (φ)	Degree	20.0	20.0	20.0	20.0	20.0
	Poisson ratio (ν)	–	0.25	0.25	0.25	0.25	0.25

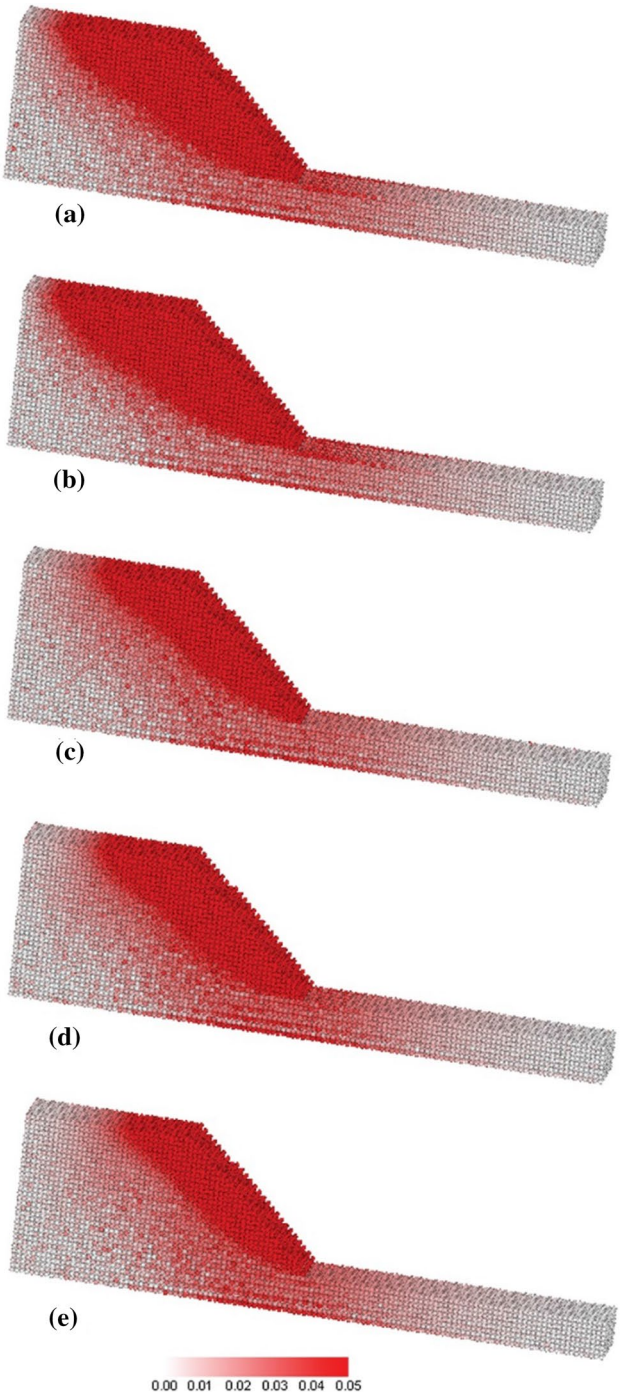

Fig. 14 Displacement contour of different non-homogeneous slopes: **a** Slope-1, **b** Slope-2, **c** Slope-3, **d** Slope-4, **e** Slope-5

minimized by adopting plausible countermeasure(s). There are several slope stability protection measures reported in books and technical writings. Slope stabilized piles and removal of unstable portion are two rational approach for mitigation of such hazard. Therefore, these two countermeasures were analyzed numerically in this study to check their effectiveness. Subsequent sections demonstrate this two countermeasure against slope collapse.

Removal of upper portion

An easy approach to prevent landslide induced collapse is the removal of some unstable soil mass from the top and applied in some real preventive strategies. A numerical slope model eliminating an upper portion was formulated and shown in Fig. 15. For simplicity, the homogeneous granular slope was considered for the countermeasure study. A section of 50 mm upper soil was removed with 2H: 1 V gradient from an existing slope model, and allowed to flow in a dam break manner. Their normalized run-out and displacement contour were plotted to check the justification of such remedial steps. Figure 16 shows normalized run-out of the stabilized slope by removing the upper portion of the existing slope. Run-out followed a decreasing trend from the start of the simulation compare to existing slopes. An approximately 6–8% run-out was reduced by removing the upper soil portion, hence, somewhat depict the usefulness of such technique. However, the flow front also depends on many factors, such as variable soil properties, the thickness of removed soil, topography etc. The study is not intended to provide insight into mitigation policy; rather, an emphasis was given on the response of naturally collapsed soil mass. Meanwhile, this countermeasure simulation may step forward towards the numerical application of several protective measures.

Slope stabilized pile

In some areas, landslide stabilized pile provides a better option than other countermeasures. Typically, RCC precast piles are driven in the unstable slope, which eventually increases the stiffness of soils and reduces the possibility of massive slope collapse. The application of retaining wall may put higher resistance than a pile. However, the construction of the long-retaining wall is not feasible in many instances. For that the simulation aimed to check the effectiveness of piles along the slope. Figure 17 shows the typical layout of slope stabilized pile. Identical properties of the previous case were considered for the comparative study of these two methods. Meanwhile, the location of the pile is important for better resistance to slope collapse. Therefore, three cases were chosen: piles placed at the lower portion of the slope, piles placed at the middle portion of the slope, and piles placed at the upper portion of the slope. Normalized run-out of all three scenarios were plotted and shown

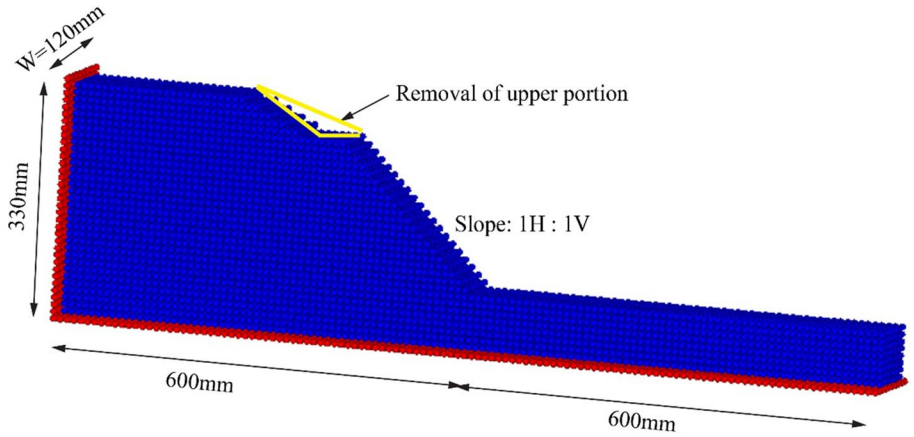

Fig. 15 Protection of slope failure by removing upper portion of slope

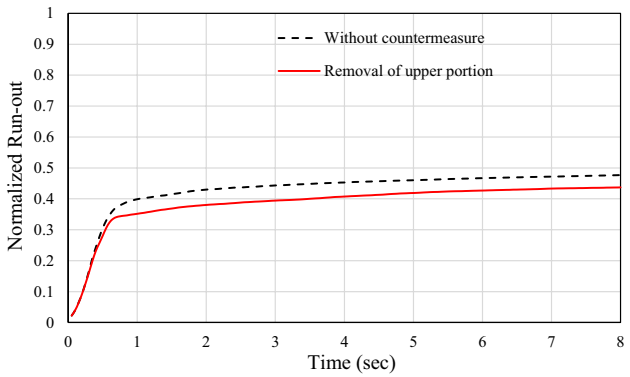

Fig. 16 Normalized run-out of slope with upper cut

in Fig. 18. It was found that placing piles at the top portion of the slope had minimal effect on the response as most of the sloped soil masses did not get any resistance. The piles located at the lower portion provided some resistance to flow as the ultimate normalized run-out reduced to a considerable distance. Nevertheless, the maximum resistance was found placing pile at the middle portion of the slope model. An approximately 20–25% of run-out reduced by applying piles at the middle portion of the slope. The displacement contour also showed narrow slip plane and useful for prevention of such slope disasters.

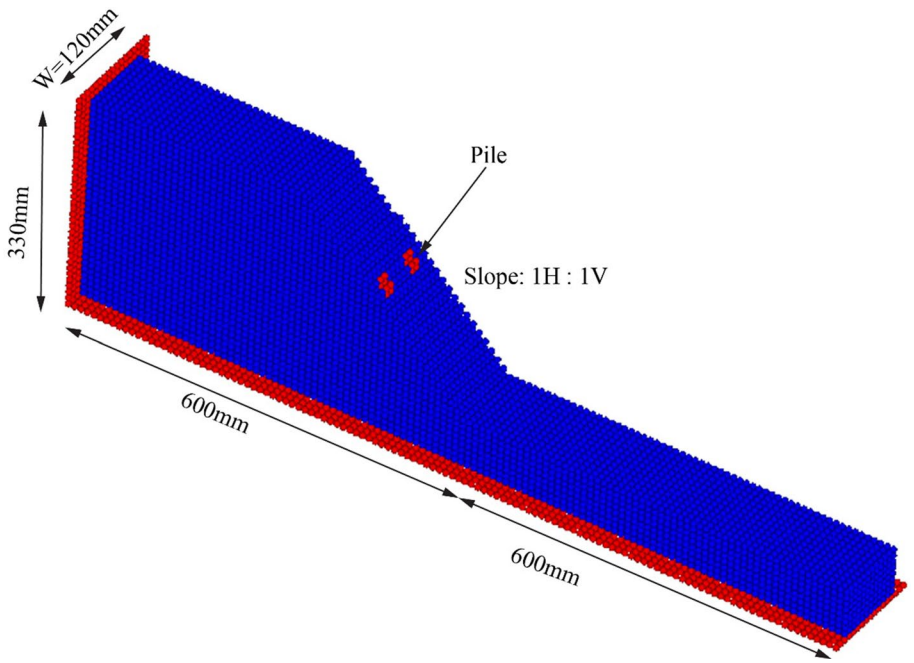

Fig. 17 Protection of slope failure by piles

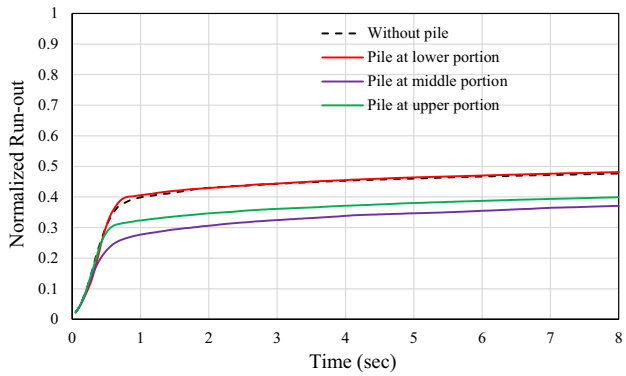

Fig. 18 Normalized run-out of slope with pile

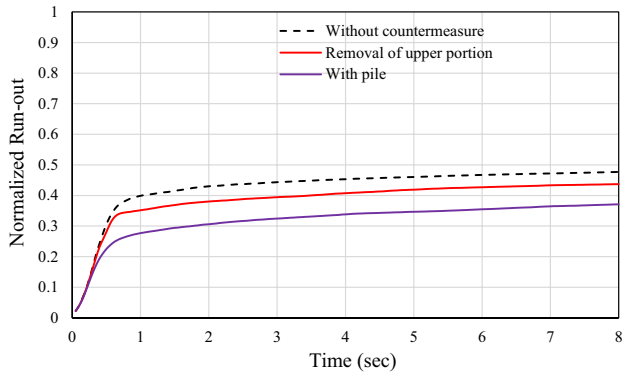

Fig. 19 Comparison between different protection measures

A comparative discussion of both types of remedial measures is shown in Fig. 19. A significant reduction to the flow was evident as about 25% of the maximum run-out reduced by utilizing piles. The final slope profile also plotted in Fig. 20, and no significant variation of the trend of the final profile was observed. In a nutshell, the above two countermeasures somewhat useful for prevention of slope induced disasters.

Conclusion

A three-dimensional numerical SPH model was developed based on elastoplastic constitutive relations to understand the natural response of slope failures. Both homogeneous and non-homogeneous slope models were simulated using the developed numerical tool. The normalized run-out of the entire slope was tracked, and compatible responses were seen. Besides, displacement contour was plotted which portray the naturally occurring slip plane and also found compatible with the assumed slip circle in LEM. The slip plane varied with a variation of properties of geo-materials. Therefore, the inherent characteristics of the slipped surface were identified. This capability of capturing inherent slope collapse put a rational estimation for mitigation policy, especially in designing anchor plates or reinforced earth wall, where the effectiveness of anchoring methods depends on identification of actual slip plane.

Furthermore, two conventional countermeasures, one is the removal of a certain upper portion of slopes, and other is slope stabilized pile were numerically checked. Reduction of normalized run-out was found in both cases, though, the slope stabilized pile provided better performance in resisting the flow of displaced mass. The displacement contour also showed a coherent response in both cases. To conclude, this paper suggested that SPH can be considered an efficient solution tool for computing displacement and flow pattern of geo-materials that are prone to failure and also capable of predicting the final slope configuration despite it has shortcomings of boundary condition. Further improvement of constitutive relations and more extensive simulations with the inclusion of sensitivity of other parameters may step up this method as a practical tool in slope stability analysis.

Fig. 20 Slope profile for different protection measures

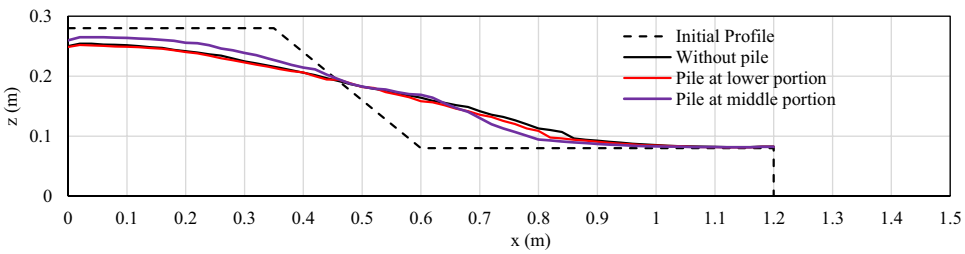

Acknowledgement Not Applicable.

Funding Not Applicable.

Compliance with ethical standard

Ethical Statement The submitted paper complies with the Ethical Standard of the journal.

References

1. De Blasio FV (2011) Introduction to the physics of landslides. Springer, New York
2. Huang YPH (2014) Slope stability analysis by the limit equilibrium method: Fundamentals and methods. ASCE Press, Reston
3. Shi B, Zhang Y, Zhang W (2018) Analysis of the entire failure process of the rotational slide using the material point method. Int J Geomech 18:1–13. https://doi.org/10.1061/(ASCE)GM.1943-5622.0001211
4. Kostić S, Vasović N, Sunarić D (2016) Slope stability analysis based on experimental design. Int J Geomech 16:1–11. https://doi.org/10.1061/(ASCE)GM.1943-5622.0000551
5. Erguler ZA, Karakuş H, Ediz IG, Şensöğüt C (2020) Assessment of design parameters and the slope stability analysis of weak clay-bearing rock masses and associated spoil piles at Tunçbilek basin. Arab J Geosci. https://doi.org/10.1007/s12517-019-5030-8
6. Pei H, Jing J, Zhang S (2020) Experimental study on a new FBG-based and Terfenol-D inclinometer for slope displacement monitoring. Meas J Int Meas Confed 151:107172. https://doi.org/10.1016/j.measurement.2019.107172
7. Helwany S (2007) Applied soil mechanics: with ABAQUS applications. Wiley, New York
8. Liu GR, Liu MB (2003) Smoothed particle hydrodynamics: a meshfree particle method. World Scientific Publishing Co. Pte. Ltd.
9. Huang Y, Dai Z, Zhang W (2014) Geo-disaster modeling and analysis: an SPH-based approach. Springer, Berlin
10. Rahman MA, Konagai K (2018) A hands-on approach to estimate debris flow velocity for rational mitigation of debris hazard. Can Geotech J 55:941–955. https://doi.org/10.1139/cgj-2017-0211
11. Islam MR, Hayano K, Rahman MA (2019) Insights into effects of seepage on failure of breakwater mound: experimental and numerical investigations. Indian Geotech J. https://doi.org/10.1007/s40098-019-00356-8
12. Islam MR, Rahman MA, Hayano K (2020) Application of smoothed particle hydrodynamics (SPH) for simulating various geotechnical problems. SN Appl Sci. https://doi.org/10.1007/s42452-020-2379-y
13. Wang G, Riaz A, Balachandran B (2019) Smooth particle hydrodynamics studies of wet granular column collapses. Acta Geotech. https://doi.org/10.1007/s11440-019-00828-4
14. Lucy LB (1977) A numerical approach to the testing of the fission hypothesis. Astron J. https://doi.org/10.1086/112164
15. Gomez-Gesteira M, Dalrymple RA (2004) Using a three-dimensional smoothed particle hydrodynamics method for wave impact on a tall structure. J Waterw Port Coastal Ocean Eng 130:63–69
16. Fang J, Owens RG, Tacher L, Parriaux A (2006) A numerical study of the SPH method for simulating transient viscoelastic free surface flows. J Nonnewton Fluid Mech 139:68–84. https://doi.org/10.1016/j.jnnfm.2006.07.004
17. Akbari H (2017) Simulation of wave overtopping using an improved SPH method. Coast Eng 126:51–68. https://doi.org/10.1016/j.coastaleng.2017.04.010
18. Crespo AJ, Gómez-Gesteira M, Dalrymple RA (2008) Modeling Dam Break Behavior over a Wet Bed by a SPH Technique. J Waterw Port Coastal Ocean Eng 134:313–320. https://doi.org/10.1061/(asce)0733-950x(2008)134:6(313)
19. Parmas B, Vosoughifar HR (2016) Novel method of boundary condition of dam-break phenomena using ghost-particle SPH. Nat Hazards 84:897–910. https://doi.org/10.1007/s11069-016-2463-1
20. Ran Q, Tong J, Shao S et al (2015) Advances in Water Resources Incompressible SPH scour model for movable bed dam break flows. Adv Water Resour 82:39–50. https://doi.org/10.1016/j.advwatres.2015.04.009
21. Shao JR, Li HQ, Liu GR, Liu MB (2012) An improved SPH method for modeling liquid sloshing dynamics. Comput Struct 100–101:18–26. https://doi.org/10.1016/j.compstruc.2012.02.005
22. Wang G, Riaz A, Balachandran B (2017) Computational studies on interactions between robot leg and deformable terrain. Procedia Eng 199:2439–2444. https://doi.org/10.1016/j.proeng.2017.09.376
23. Ghadampour Z, Hashemi MR, Talebbeydokhti N et al (2015) Some numerical aspects of modelling flow around hydraulic structures using incompressible SPH. Comput Math Appl 69:1470–1483. https://doi.org/10.1016/j.camwa.2015.04.001
24. Zheng X, Duan WY (2010) Numerical simulation of dam breaking using smoothed particle hydrodynamics and viscosity behavior. J Mar Sci Appl 9:34–41. https://doi.org/10.1007/s11804-010-8037-9
25. Ferrari A, Dumbser M, Toro EF, Armanini A (2009) A new 3D parallel SPH scheme for free surface flows. Comput Fluids 38:1203–1217. https://doi.org/10.1016/j.compfluid.2008.11.012
26. Dalrymple RA, Rogers BD (2006) Numerical modeling of water waves with the SPH method. Coast Eng 53:141–147. https://doi.org/10.1016/j.coastaleng.2005.10.004
27. Jian W, Liang D, Shao S et al (2015) SPH study of the evolution of water–water interfaces in dam break flows. Nat Hazards 78:531–553. https://doi.org/10.1007/s11069-015-1726-6
28. Ferrari A (2010) SPH simulation of free surface flow over a sharp-crested weir. Adv Water Resour 33:270–276. https://doi.org/10.1016/j.advwatres.2009.12.005
29. Chang TJ, Kao HM, Chang KH, Hsu MH (2011) Numerical simulation of shallow-water dam break flows in open channels using smoothed particle hydrodynamics. J Hydrol 408:78–90. https://doi.org/10.1016/j.jhydrol.2011.07.023
30. Ghaïtanellis A, Violeau D, Ferrand M et al (2018) A SPH elastic-viscoplastic model for granular flows and bed-load transport. Adv Water Resour 111:156–173. https://doi.org/10.1016/j.advwatres.2017.11.007
31. Bui HH, Fukagawa R, Sako K, Ohno S (2008) Lagrangian meshfree particles method (SPH) for large deformation and failure flows of geomaterial using elastic–plastic soil constitutive model. Int J Numer Anal Methods Geomech 32:1537–1570. https://doi.org/10.1002/nag
32. Zhu C, Huang Y, Zhan LT (2018) SPH-based simulation of flow process of a landslide at Hongao landfill in China. Nat Hazards 93:1113–1126. https://doi.org/10.1007/s11069-018-3342-8
33. Huang Y, Dai Z, Zhang W, Chen Z (2011) Visual simulation of landslide fluidized movement based on smoothed particle hydrodynamics. Nat Hazards 59:1225–1238. https://doi.org/10.1007/s11069-011-9859-8

34. Dai Z, Huang Y, Cheng H, Xu Q (2014) 3D numerical modeling using smoothed particle hydrodynamics of flow-like landslide propagation triggered by the 2008 Wenchuan earthquake. Eng Geol 180:21–33. https://doi.org/10.1016/j.enggeo.2014.03.018
35. Dai Z, Huang Y, Cheng H, Xu Q (2017) SPH model for fluid–structure interaction and its application to debris flow impact estimation. Landslides 14:917–928. https://doi.org/10.1007/s10346-016-0777-4
36. Nguyen CT, Nguyen CT, Bui HH et al (2017) A new SPH-based approach to simulation of granular flows using viscous damping and stress regularisation. Landslides 14:69–81. https://doi.org/10.1007/s10346-016-0681-y
37. Huang Y, Cheng H, Dai Z et al (2015) SPH-based numerical simulation of catastrophic debris flows after the 2008 Wenchuan earthquake. Bull Eng Geol Environ 74:1137–1151. https://doi.org/10.1007/s10064-014-0705-6
38. Wang W, Chen G, Han Z et al (2016) 3D numerical simulation of debris-flow motion using SPH method incorporating non-Newtonian fluid behavior. Nat Hazards 81:1981–1998. https://doi.org/10.1007/s11069-016-2171-x
39. Braun A, Cuomo S, Petrosino S et al (2018) Numerical SPH analysis of debris flow run-out and related river damming scenarios for a local case study in SW China. Landslides 15:535–550. https://doi.org/10.1007/s10346-017-0885-9
40. Hu M, Liu MB, Xie MW, Liu GR (2015) Three-dimensional run-out analysis and prediction of flow-like landslides using smoothed particle hydrodynamics. Environ Earth Sci 73:1629–1640. https://doi.org/10.1007/s12665-014-3513-1
41. Rahman MA, Konagai K (2017) Substantiation of debris flow velocity from super-elevation: a numerical approach. Landslides 14:633–647. https://doi.org/10.1007/s10346-016-0725-3
42. Monaghan JJ, Lattanzio JC (1985) A refined particle method for astrophysical problems. Astron Astrophys 149:135–143
43. Lube G, Huppert HE, Sparks RSJ, Hallworth MA (2004) Axisymmetric collapses of granular columns. J Fluid Mech. https://doi.org/10.1017/S0022112004009036
44. Rahman MA (2016) Ascertaining a hands-on approach to estimate debris flow velocities for rational debris hazard mitigation. PhD Diss Yokohama Natl Univ